Landslides (2018) 15:2227–2241
DOI 10.1007/s10346-018-1035-8
Received: 12 December 2017
Accepted: 29 June 2018
Published online: 9 July 2018

Mingjing Jiang · Zhifu Shen · Di Wu

CFD-DEM simulation of submarine landslide triggered by seismic loading in methane hydrate rich zone

Abstract Submarine landslide due to seismic loading in methane hydrate-rich zone was simulated in this study using coupled computational fluid dynamics and discrete element method. Dynamic features and Magnus force were incorporated in the coupling scheme to improve the simulation fidelity in dynamic problem. A sinusoidal type seismic loading was applied to a steep submarine slope, which was characterized by a strong inter-layer of methane hydrate-bearing sediments. The simulation results show that a flow-type sliding occurs and the sliding ends with a gentle slope of accumulated debris material. The fluid flows in an eddy pattern near the sliding mass. The presence of methane hydrate can increase the strength and decrease the damping of the sediment. When MH saturation is low (25 and 30%), the combined seismic loading and particle-fluid interaction damage the MH-rich layer, which allows settlement behind the slope crest and upheaval in front of the slope toe. The two ground deformation patterns (settlement and upheaval) are not observed when MH saturation is high (40 and 50%) because the sediment strength is great enough to resist seismic damage. The lower damping in higher MH saturation sediment allows more energy to be transferred from ground base to potential sliding mass and consequently the sliding initiates earlier. Implications of the simulation results in the assessment of earthquake-induced submarine hazards are discussed.

Keywords Submarine landslide · Earthquake · Methane hydrate bearing sediment · CFD-DEM simulation

Introduction

Methane hydrate (MH) is an ice-like crystalline solid composed of methane molecules captured in hydrogen-bonded water cages. MH is formed at relatively high-pressure and low-temperature conditions (Kvenvolden and Lorenson 2001). As a promising energy source, MH was found to grow in various forms in the marine sediments, including dissemination, nodule, vein, veinlet, and layer forms (Tréhu et al. 2003). The dissemination form is usually discovered in coarse-grained sediments and can be further divided into pore filling, load bearing, grain coating, and cementing structures (Kingston et al. 2006). MH can increase the strength and stiffness of the host sediments especially when it is in a cementing structure usually formed under conditions of high gas flux and coarse-grained sediments (Dvorkin et al. 1999; Ebinuma et al. 2005; Masui et al. 2005; Winters et al. 2007; Miyazaki et al. 2011; Hyodo et al. 2013), which are also favorable conditions for hydrate exploitation (Valdes and Santamarina 2007; Boswell and Collett 2011).

Human activities (e.g., heat produced in drilling, oil flowing within pipelines) and natural processes, such as thermohaline circulation (Bice and Marotzke 2002), deep sea warming (Bains et al. 1999), and mantle-derived intrusion (Svensen et al. 2004), can increase seafloor temperature, sequentially melt hydrate bonds between sediment grains and inevitably degrade the mechanical properties of sediments. Besides, continental margins are seismicity active area with frequent earthquakes and ocean currents. Earthquake can exert horizontal inertial forces on slope and inducing excess pore water pressure (Wright and Rathje 2003). These natural and human-related activities could trigger intensive submarine landslides along the continental margins in MH-rich areas.

Submarine landslides are often accompanied with massive sediment transport with large runout distance. It is speculated that the Storegga slide was potentially triggered by thermal dissociation of MH (Mienert et al. 2005; Solheim et al. 2005); a total volume of nearly 5000 km^3 traveled 140 km from the western Norway to southern Iceland (Harbitz 1992). Sediment transport poses a great threat to artificial facilities in the ocean. The submarine landslides and turbidity currents associated with the 2006 Pingtung earthquake off SW Taiwai were reported to cut off the communication connection between Southeast and East Asian countries (Hsu et al. 2008). Cable ruptures and communication losses were caused by the 1992 Grand Banks earthquake (Heezen and Drake 1964; Hasegawa and Kanamori 1987), the 1954 Orléansville earthquake (Heezen and Ewing 1955), and the 1980 El-Asnam earthquake (El-Robrini et al. 1985), among others. Three offshore oil platforms on the Mississippi Delta were damaged by submarine landslides triggered by large storm waves due to the 1969 Hurricane Camille (Bea 1971). Some catastrophic tsunamis are believed to be associated with massive submarine landslides (Uri et al. 2009; Goff and Terry 2016; Yavari-Ramshe and Ataie-Ashtiani 2017), including the Grand Banks earthquake-induced submarine landslide (Fine et al. 2005), landslides in Papua New Guinea (Tappin et al. 2001), and the 1918 western Puerto Rico submarine landslide (Lopez-Venegas et al. 2008).

Submarine landslides are rare in frequency and vast in area. It is inaccessible to directly track their initiation, development, and re-stabilization. The geomorphology of submarine landslide was usually identified from bathymetric measures and seismic stratigraphy, including landslide area, runout distance, slope gradient, and headscarp (Masson et al. 1993; McAdoo et al. 2000). The landslide initiation and development process can be only back-analyzed by tracking changes in depositional structures or the sequence of damages (e.g., loss of communication; Hsu et al. 2008). The mechanisms of gentle slope failure and long runout distance are still not well understood.

Historical analyses suggest that earthquakes triggered most of the large submarine landslides (Masson et al. 2006). To understand the mechanism and process of submarine landslide due to earthquake, theoretical analyses and numerical simulations had been widely used to study landslide dynamics with different causes and under various geological conditions. Limit equilibrium method is the most widely used because of its simplicity. Locat et al. (2004) found that the absence of transition from landslide

initiation to post-failure flow in the limit equilibrium approach cannot properly predict the size of landslide-induced tsunami. Biscontin et al. (2004) performed finite element simulation of the seismic site response with a simplified model for clay; site responses including excess pore water pressure, acceleration, and displacement can be utilized to understand the triggering mechanism. Site profile and sediment stratification effects can be conveniently studied by finite element simulations due to the flexibility in assigning different parameters to elements. The mass transport mechanism is the key in assessing hazards of submarine landslides (Locat and Lee 2002). Finite element simulation cannot reproduce the large mass flow after slope failure. With the aid of computational fluid dynamics coupled with the discrete element method (CFD-DEM), submarine landslide initiation, mass transport, and depositing process can be completely simulated as a natural result of solid-fluid interaction. In the simulated MH dissociation-triggered submarine landslide by Jiang et al. (2015), four types of slides (fall, flow, slump-flow, and slump) were reproduced, whose occurrence depends on the location and extend of MH dissociation.

Due to the advantages of CFD-DEM simulation in reproducing the complete sliding process, this coupling method is used in this study to simulate seismic loading-triggered submarine landslide in MH-rich zone. The CFD-DEM computation scheme will be first introduced briefly. Then, the slope geometry and test conditions will be discussed. The effects of MH saturation on the submarine slope instability will be analyzed in terms of mass transport, MH bond damage, and excess pore water pressure. The implications of the simulation results in the assessment of earthquake-induced disaster will be discussed finally.

CFD-DEM coupling computation

The CFD-DEM coupling scheme in this study is a continuum-discrete approach. The fluid flow is simulated by solving Navier–Stokes (N-S) equation based on the concept of coarse-grid local average in CFD, and the motion of each individual particle is obtained by solving Newton's second law of motion in DEM. CFD and DEM are coupled through exchanging particle-fluid interaction. The coupling computation scheme has been introduced in detail by Jiang et al. (2015). To simulate seismic loading-induced submarine landslide in this study, two aspects in the coupling computation were improved: (1) the contact model in DEM was extended to incorporate dynamic features and (2) Magnus force in fluid-particle interaction was considered. The two aspects are briefly introduced here and complete descriptions will be covered in a forthcoming publication (Jiang et al. 2018a).

It should be noted that the DEM simulations in this study are 2D with disk particles. On the CFD side, the formulations are basically for 3D but the flow velocity in the out-of-plane direction is set zero. That is, 2D flow is considered in this way. For the CFD-DEM coupling, 2D disks are fictitiously treated as spheres with the same diameter and velocity. The fictitious 3D sphere assemble is used to determine porosity and particle volume that are needed to calculate the interaction forces between particle and fluid. The interaction forces are then sent to CFD and DEM to be directly used for fluid and particle movement calculations. This choice is because the MH bond contact model is in 2D and a 3D model is under development. Although it is not physically accurate, this choice can capture the general trend of fluid-particle interaction.

Dynamic features of the contact model

In our two-dimensional DEM simulation of methane hydrate-bearing sediments (MHBS), the material was regarded as a collection of disks bonded by MH at contacts, representing a cementing structure among the four typical types of MHBS structures (i.e., pore filling, load bearing, grain coating, and cementing). The MH material was not explicitly simulated but its mechanical effects were considered in the bond contact model. Previous static bond contact model was developed by adding MH bonding effects into an unbonded contact mode (Jiang et al. 2014, 2015, 2016). The bonding effects depend on the strength of MH material. Two dynamic features have to be considered to extend the static contact model for a dynamic problem.

(1) Rate dependency of MH strength. A MH bond can break under combined normal force (in tension or compression), shear force, and rolling moment. The bond strength is controlled by the material strength of MH which can be obtained from experiments. Triaxial compression tests on pure MH bulk sample show that the shear strength of MH depends on temperature, confining pressure, sample density, and loading rate (Hyodo et al. 2002, 2005; Nabeshima et al. 2005; Song et al. 2010; Yu et al. 2010). The first three factors have been discussed and incorporated into the previous static bond contact model and applied in DEM simulations (2D simulation (Jiang et al. 2015), 3D simulation (Shen and Jiang 2016)). As for the loading rate effect, Figure 1 shows that the peak shear strength of MH increases with the logarithm of axial strain rate in an almost linear way. The peak strength q_{max} (MPa) was fitted and implemented into the dynamic bond contact model used in this study:

$$q_{max} = q^{*}_{max}(T, \sigma_w) + \xi \log \dot{\varepsilon}_1 \quad (1)$$

where $q^{*}_{max}(T, \sigma_w)$ (MPa) is the peak shear strength when the axial strain rate $\dot{\varepsilon}_1$ is 1%/min, which depends on σ_w, the confining pressure in triaxial compression test, and T is the temperature. The parameter ξ (MPa) is not a constant but depends on temperature and confining pressure:

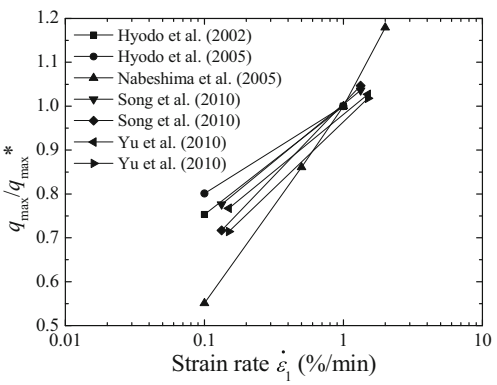

Fig. 1 Rate dependency of MH strength

$$\xi = a\sigma_w\left(\frac{T}{T^*}+b\right) \tag{2}$$

where $T^* = 237$ K and $a = -3.7$ and $b = -1.0$ are the constants fitted from experimental data. In this fitting equation, the confining pressure σ_w is in MPa and the temperature T is in K.

(2) Different normal stiffness for loading and unloading in unbonded contact model after MH breakage. The mechanical responses of the unbonded inter-particle contact are shown in Fig. 2. This unbonded contact model replaces the bond contact model after MH breakage. The model includes normal, tangential, and rolling interactions (Jiang et al. 2005, 2018b). In Fig. 2, K_n^p and K_{un}^p are the normal loading and unloading stiffnesses, respectively, and μ^p is the inter-particle friction coefficient. In the normal direction, the loading stiffness is different from the unloading stiffness and their ratio $s_p = K_n^p/K_{un}^p$ has been studied theoretically (Thornton et al. 2013) and experimentally (Imre et al. 2008). In this way, dynamic plastic energy dissipation induced by particle collision was considered. This stiffness change was not considered in the tangential (stiffness K_s^p) and rolling (stiffness K_m^p) directions. The rolling stiffness was first derived by Jiang et al. (2005),

$$K_m^p = K_n^p\left(\beta^p\overline{\mathrm{R}}\right)^2/12 \tag{3}$$

where $\overline{R}$ is the average radius of the two particles in contact and β^p is a shape parameter used to measure particle angularity effects.

The rolling resistance in Fig. 2 was derived by Jiang et al. (2005) as

$$M^p \le F_n^p\beta^p\overline{\mathrm{R}}/6 \tag{4}$$

where F_n^p is the normal force.

Damping is critical in dynamic problem and is repeated here, although it has been considered in the static contact model. Linear viscous damping was used to dissipate kinematic energy. The normal, tangential, and rotational viscous damping forces/moment can be calculated as

$$F_n^v = c_n\dot{u}_n \tag{5a}$$

$$F_s^v = c_s\dot{u}_s \tag{5b}$$

$$M^v = c_r\dot{\theta} \tag{5c}$$

where c_n, c_s, and c_r are the normal, tangential, and rotational viscous damping coefficients, respectively, and $\dot{u}_n$, $\dot{u}_s$, and $\dot{\theta}$ are the normal, tangential, and rotational rates, respectively. The damping coefficients can be calculated by

$$c_n = r_n c_n^{crit} \tag{6a}$$

$$c_s = r_s c_s^{crit} \tag{6b}$$

$$c_r = \left(\overline{R}\beta^p\right)^2 c_n/12 \tag{6c}$$

where r_n and r_s are two parameters and c_n^{crit} and c_s^{crit} are the normal and tangential critical damping constants:

$$c_n^{crit} = 2\sqrt{mK_n^p} \tag{7a}$$

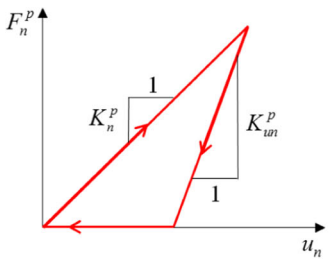

(a) Normal direction

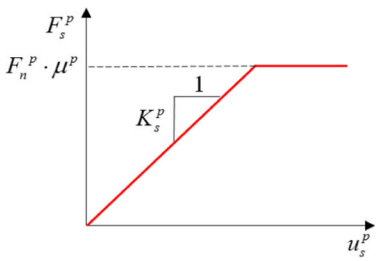

(b) Tangential direction

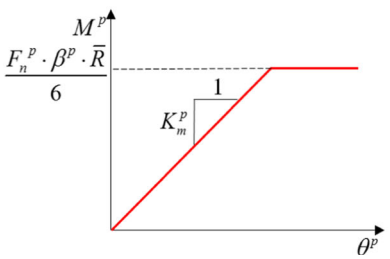

(c) Rolling direction

Fig. 2 Mechanical responses in the unbonded contact model

$$c_s^{crit} = 2\sqrt{mK_s^p} \tag{7b}$$

where m is the effective system mass which is the disk mass in the case of a disk-wall contact, or equals to $m_1m_2/(m_1 + m_2)$ in the case of a disk-disk contact (m_1 and m_2 are the masses of the two disks).

Magnus force in fluid-particle interaction

In addition to the pressure difference force and drag force considered by Jiang et al. (2015), Magnus force was considered in the fluid-particle interaction here. Magnus force comes from particle rotation in fluid. As shown in Fig. 3, u_r is the relative translational velocity between a particle and the fluid and ω is the angular velocity of the particle. Tsuji et al. (1985) proposed an equation to calculate Magnus force based on experimental results:

$$F_M = C_M\pi\rho_f u_r^2 d^2/8 \tag{8a}$$

$$C_M = f(\Gamma) \tag{8a}$$

$$\Gamma = \omega d/(2u_r) \tag{8b}$$

where C_M is the Magnus coefficient, ρ_f is the fluid density, d is the particle radius, and Γ is a dimensionless angular velocity.

Rubinow and Keller (1961) derived a theoretical solution of Magnus coefficient in low Reynolds number case (< 1): $C_M = 2\,\Gamma$. Tsuji et al. (1985) and Barkla and Auchterlonie (1971) experimentally obtained a series of data on the relationship between C_M and Γ. These data were used to fit an empirical relationship as shown in Fig. 4:

$$C_M = 0.26\Gamma^{0.45} \tag{9}$$

Single-particle ejection test was simulated to examine the effects of Magnus effects. Following the work by Tsuji et al. (1985), the numerical ejection test setup is shown in Fig. 5a. The test parameters were chosen as $V_x = 20$ m/s, $V_y = 10$ m/s, and $\omega = 200$ rad/s. The viscous coefficient of the fluid is 0.001 Pa s, fluid density is 1000 kg/m^3, and the particle density is 1040 kg/m^3. Figure 5b shows that the Magnus force has a significant effect on the trajectory of particle. Since the magnitude of particle speed is around 10 m/s in our simulated landslide (to be discussed below), it seems necessary to incorporate this Magnus effect.

Although limited numerical simulations have revealed the effects of neighboring particles on Magnus force (Zhou and Fan 2015), there has not been a complete equation to consider such effect (especially considering the random angular velocity) so far. Therefore, the Magnus force not considering neighboring particle effects was used in this study as an approximation.

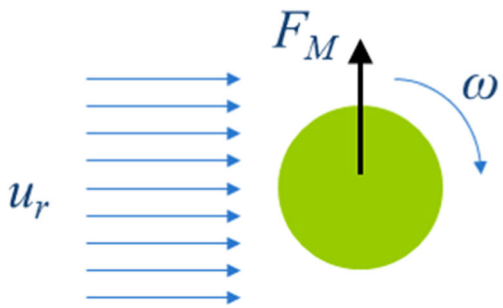

Fig. 3 Magnus force

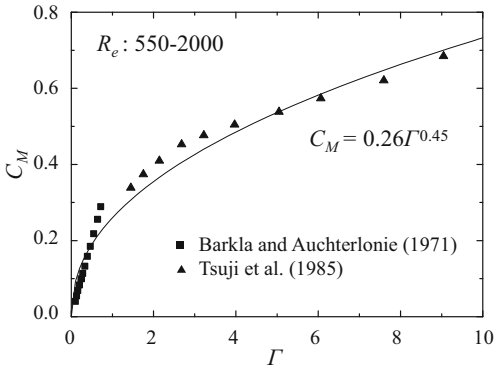

Fig. 4 Relationship between C_M and Γ

Submarine landslide simulation

Based on the continental margin in the northern South China Sea, a hypothetical subaqueous slope model was established in Fig. 6. The gravity was chosen to be Ng ($N = 1000$ here), and correspondingly, the model geometry size was scaled down to $1/N$ (=1/1000) to reduce the particle number for efficiency. Many failed continental margins have an inclination range from a few degrees to 20°. However, some relative steep submarine slopes do exist and they become the most dangerous cases under earthquake. In this study, a steep slope (45°) was simulated as an unfavorable case. The grains in the slope were composed of ten classes of disks with $d_{max} = 9.0$ mm, $d_{50} = 7.6$ mm, and $d_{min} = 6.0$ mm, as shown in Fig. 7. The particle size choice is a balance of computation resource and simulation resolution. In the prototype model, the crest and toe of the slope are at a depth of 1000 and 1600 m beneath the sea level, respectively. The right side boundary of the ground is 1400 m ($184d_{50}$) away from of the slope toe. The 150 m ($20d_{50}$) thick hydrate zone extends along the slope and is 100 m ($13d_{50}$) below the slope surface. The 7000 × 3200-m fluid domain was discretized into 269 × 123 rectangular cells for fluid computation with all the boundaries being static hydraulic pressure boundaries.

The sea bottom temperature T_o of South China Sea is usually 2°~6° and the ground thermal gradient d_t is 32~40°/km (Luo et al. 2013). The temperature T_h at depth h below the seabed can be calculated by

$$T_h = T_o + d_t h \tag{10}$$

This paper assumes that T_o equals to 4° and d_t is 36°/km. During submarine landslide, the temperature in the hydrate zone is assumed to be constant. According to the model geometry, the static hydraulic pressures at the crest and toe of the submarine slope are 10 and 16 MPa, respectively. MH at a particle contact is exposed to ambient pore fluid. The pore water pressure plays a similar role to confining pressure in triaxial compression test on bulk MH material. Therefore, the in situ pore water pressure and

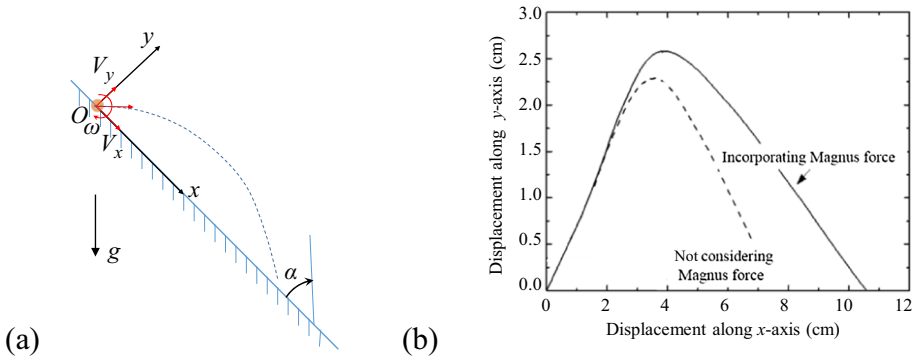

Fig. 5 CFD-DEM simulation of particle ejection test. **a** Ejection test setup. **b** Particle motion trajectory with and without Magnus force

the ground temperature enters Eq. (1) to determine MH strength and thus the MH bonding effects.

The MHBS material in the hydrate zone was described by the dynamic MH bond contact model briefly introduced above, and the key parameters of the model are shown in Table 1. The complete physical meanings of the parameters are explained in detail in Jiang et al. (2015). The model parameters were determined based on qualitative comparison with experimental results on artificial MHBS (Hyodo et al. 2013). For material outside the hydrate zone, the behavior was described by a built-in contact bond model in PFC2D. The normal and tangential strengths of this built-in bond model are 1 kN/m, calibrated against the macroscopic strength of weakly bonded sandy samples encountered in South China Sea (Zhang and Luan 2013).

The fluid parameters were given based on the field investigation of the hydraulic conditions of South China Sea (Luo et al. 2013). The viscous coefficient of fluid was calibrated to ensure that the velocity of a free-fall ball respects the chosen similarity ratio.

The seismic loading was chosen based on earthquake history data in South China Sea, where the exciting peak acceleration varied between 0.05 and 0.6 g. The main exciting frequency was 3 Hz (Shamy and Zeghal 2007; Shamy and Denissen 2010; Zhou et al. 2014). The seismic loading used in this study is described in Fig. 8. The peak acceleration increases linearly within the first 15 cycles, keeps constant (0.5 g) in the following 20 cycles, and finally decreases linearly to zero in the final 10 cycles. The total exciting duration is 15 s.

The simulation procedure includes five steps: (1) a rectangular DEM slope domain was prepared in a box by the multilayer under-compaction method proposed by Jiang et al. (2013) to mimic the one-dimensional deposition process; (2) extra particles were deleted to obtain the predefined slope profile; (3) particles were allowed to reach equilibrium under 500 g and the built-in bond contact model was applied; (4) the built-in bond contact model in the hydrate zone was replaced by the dynamic MH bond contact model to simulate MHBS and the ground was consolidated under a gravity of 1000 g, representing the rapid depositional process after the formation of methane hydrate; and (5) CFD module was activated and the horizontal acceleration given in Fig. 8 was applied to the soil box. The fluid did not interact with the box wall. The contact behavior between soil particle and the box wall was described by the unbonded contact model, in which the viscous damping can absorb energy to eliminate wave reflection along the boundaries.

Simulations were carried out with MH saturation of 25, 30, 40, and 50% to investigate the effects of MH saturation. MH saturation controls the size of inter-particle bond and thus determines the magnitude of bonding effects (Jiang et al. 2014, 2016).

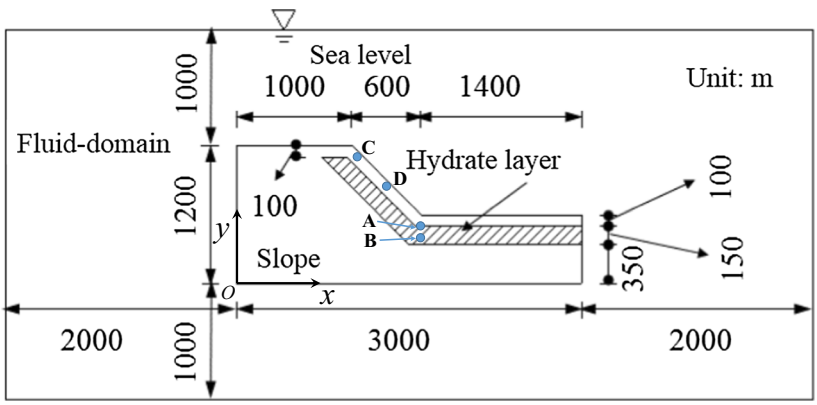

Fig. 6 Schematic diagram of the simulated slope model (unit: m)

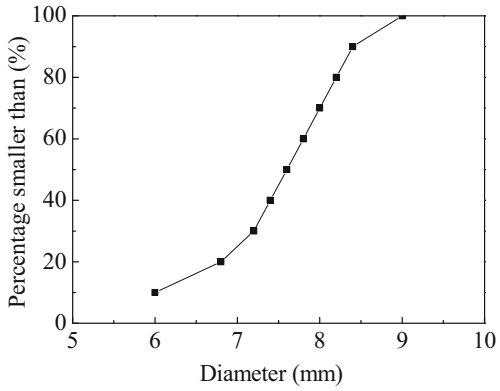

Fig. 7 Distribution of particle size

Landslide process

The complete submarine landslide process is firstly analyzed under a MH saturation of 25%. The accelerations at two points (point A at 100 m below the slope toe and point B at 200 m below the slope in Fig. 6) were monitored throughout the simulations. At each point, the average acceleration of 10 particles around the point is used as representation. Figure 8b, c presents the acceleration history of the two points. Before $t = 4.5$ s, the acceleration is very small; after that, the acceleration sharply increases up to 0.9 g for point A and 0.8 g for point B within $t = 15$ s. Soon after the excitation ends, the acceleration abruptly drops and then gradually rests. The displacements of two balls at points C and D in Fig. 6 (just below the slope surface) were monitored. Both balls slide downward along the slope. There exist clear accelerating and decelerating stages and more than half of the displacement occurs after the excitation ends, as shown in Fig. 8d. The displacements reach steady after $t = 50$ s.

Figure 9 presents the evolutions of slope profile together with spatial distributions of MH bond, particle velocity, fluid velocity, and excess pore water pressure. The MH bonds are represented by lines connecting the centroids of two particles that are cemented by a MH bond. Dash lines are superimposed in the figures to indicate the MHBS area.

Table 1 Parameters used in the coupled CFD-DEM simulation

Property	Value
Grain density (kg/m^3)	2600
Particle size (mm)	6–9
Average grain diameter (mm)	7.6
Initial planar void ratio	0.27
Normal stiffness K_{np} (N/m)	6×10^8
Shear stiffness K_{sp} (N/m)	4×10^8
Inter-particle friction μ^p	0.5
Inter-particle rolling resistance β^p	0.5
Initial density of fluid (kg/m^3) (under standard atmosphere pressure)	1000
Viscous coefficient of fluid (Pa s)	0.001
Fluid salinity	3.5%
Hydraulic conductivity (m s^{-1})	0.655

After a seismic loading for 5 s in Fig. 9a, particle movements mainly concentrate in zone A (slope toe) and in zone B (a local zone in front of the toe) as indicated by the particle velocity field. In zone A, a flow-type landslide starts with downward movement of particles. The circulation of fluid forms an eddy in the vicinity of the slope surface. The fluid flows from the slope toe to the crest above the slope surface and vice versa below the slope surface. In zone B, particles move upward with water flowing out of the ground. MH bond breakage initiates in zone B, indicated by the decrease of MH bond density. Positive excess pore water pressure is generated in zone B, and negative excess pressure is observed at the slope crest.

After a seismic loading of 12 s, massive flow-type sliding of particles is observed and the fluid flow mainly occurs near the sliding mass, as presented in Fig. 9b. The particle motions and fluid flow in zone B are much less significant than the massive landslide. Ground upheaval is observed in zone B because (1) the breakage of MH bond in zone B due to seismic loading frees the particles of MHBS and (2) excess pore pressure generated around zone B causes upward flux which exerts uplift forces on the disturbed/damaged MHBS layer. Apart from the upheaval and slope surface sliding, lateral (i.e., rightward) deformation of ground initiates in this stage and it can be clearly observed at $t = 15$ s in zone C, as shown in Fig. 9b, c. This behavior is explained as follows. Under the combined lateral earthquake load and fluid force (arising from the rightward fluid flow) exerted on the inclined MHBS layer along the slope, MH bond breakage occurs near the mid-slope, as indicated by the reduced MH bonds in zone C in Fig. 9b, c. The release of particle freedom in zone C allows particles on the left side of the slope surface to move towards the slope surface under earthquake load and fluid actions. This ground deformation then leads to top surface settlement behind the slope crest. Actually, the bond breakage in zone C initiates as early as $t =$ 5 s. The breakage accumulates until $t = 15$ s to a degree that noticeable particle motions can be observed from the distortion of "grids" of the ground. However, these lateral motions are much smaller than the dominant sliding movement.

After a seismic loading for 15 s, the crest part of the slope regains stability without noticeable particle velocity and a gentle slope is formed, as presented in Fig. 9c. The overall eddy type fluid flow does not change. There is no further development in upheaval at zone B, but at zone D, the upward fluid flux leads to the second local area with upheaval particle movement. This is because the concentrated upward fluid flow now transfers from zone B to zone D and what happens to zone B now happens to zone D. Although earthquake ends at $t = 15$ s, the sliding movement is still significant.

As illustrated in Fig. 9d, at $t = 500$ s, the slope almost regains stability with only some random particles on the slope surface moving downward. Based on the magnitude of movement, mass transport during the surface sliding is primary and the secondary movements include top ground surface settlement behind the slope crest and ground upheavals in front of the slope toe. The lateral movement inside the slope body can be identified from the distorted ground grids. Bond breakage due to earthquake and fluid action are responsible for these secondary particle movements. Note that, although the particles regain stability at $t =$

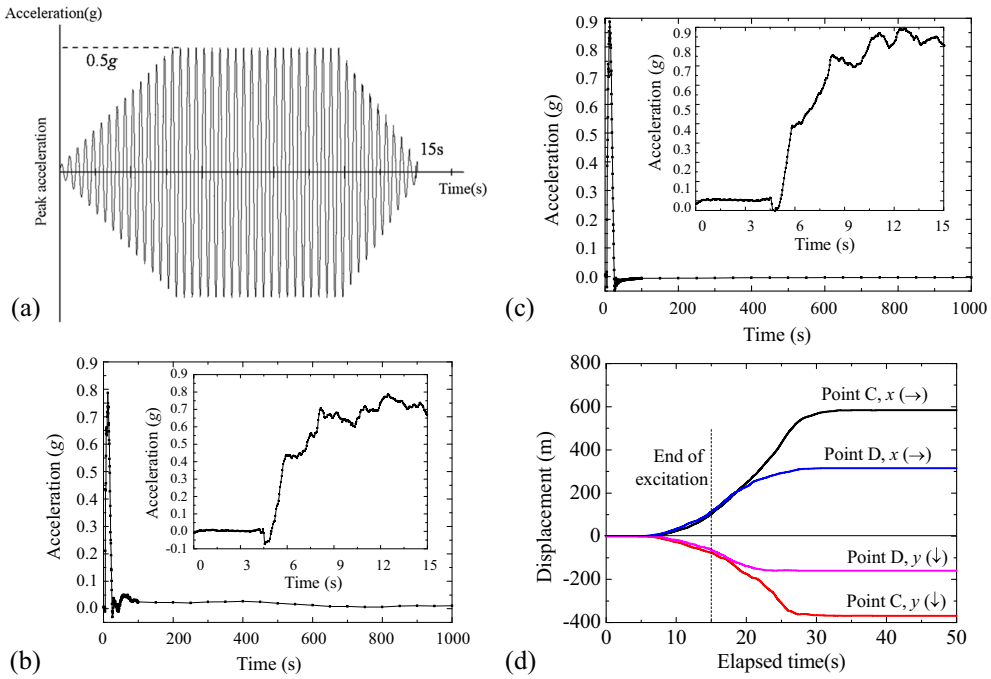

Fig. 8 Acceleration history and displacement responses. **a** Input excitation. **b** Acceleration at point A (100 m below the slope toe). **c** Acceleration at point B (200 m below the slope toe). **d** Displacements at points C and D (the arrows indicate the displacement directions in the system of Fig. 6)

500 s, the fluid is far from being static. As shown in Fig. 9d, the fluid flow mainly occurs in a narrow band immediately above the re-stabilized deposits, extending from the slope crest to the front of the accumulated debris with the fluid velocity increasing along the path. The maximum fluid velocity is found in front of the accumulated debris. The previously observed elongated eddy now becomes a sub-rounded eddy above the fluid flow band. The eddy then develops into a round eddy with a similar size to the slope height and travels fast away from the slope, as presented in Fig. 9e. The excess pore water pressure is much lower when $t > 500$ s than when $t < 15$ s.

The generation of excess pore pressure is further analyzed below. (1) The seismic responses of the slope include local contraction or dilation tendency accompanied with local plastic deformation and bond damage. This could lead to positive or negative excess pore pressure with a magnitude within 10 kPa, as implied by the excess pore pressure distribution in Fig. 9a. This source of excess pore pressure lasts until the excitation ends at $t =$ 15 s. (2) Besides, in Fig. 9a, the seismic loading breaks the horizontal MHBS layer at zone B and the consequent contraction (due to loss of bonding effects) leads to positive excess pore pressure and upward flux. (3) As indicated by the particle velocity plot in Fig. 9, the mass sliding velocity magnitude is not uniform along the slope, although the general direction is parallel to the slope inclination. The variable sliding velocities of particles lead to local contraction and dilation and thus cause positive and negative excess pore pressure near the slope, respectively. (4) When $t =$ 15 s, the ground surface settlement behind the slope crest is responsible for the positive excess pore pressure within the ground. When the excitation ends, the excess pore pressure drops quickly and stays at a level of several kPa thereafter.

Figure 10a presents the spatial distribution of normalized Magnus force (F_M/W, where W is the particle weight). Most particles experience a normalized Magus force smaller than 0.01. Particles on top layer of the sliding mass have higher angular velocity and thus experience a normalized Magus force greater than 0.05, which accounts for 0.524% of the total particle number. Figure 10b presents the frequency histogram of these high-angular-velocity particles, which concentrates within 0.1. Some randomly high values greater than 0.2 are also observed. It seems necessary to consider Magnus force if high angular velocity is expected. By comparison with simulation results without Magnus force, the general slope sliding pattern and the effects of MH saturation do not change if Magnus force is not considered, but the runout distance decreases slightly.

Effects of MH saturation

In this section, the effects of MH saturation on submarine landslide and the mechanisms are analyzed based on the simulation results.

Maximum velocity evolution

The variations of the maximum particle velocity throughout sliding are presented in Fig. 11 for different MH saturation cases. Overall, the maximum particle velocity increases with time until it reaches a peak at around $t = 50$ s and then decreases gradually to approximate zero at $t = 2000$ s. The velocity develops the fastest in the MH50 (MH saturation = 50%, similarly hereinafter) case and the slowest in the MH30 case. The peaks of the maximum particle velocity are very close for MH25, MH40, and MH50 cases, which are all higher that in the MH30 case.

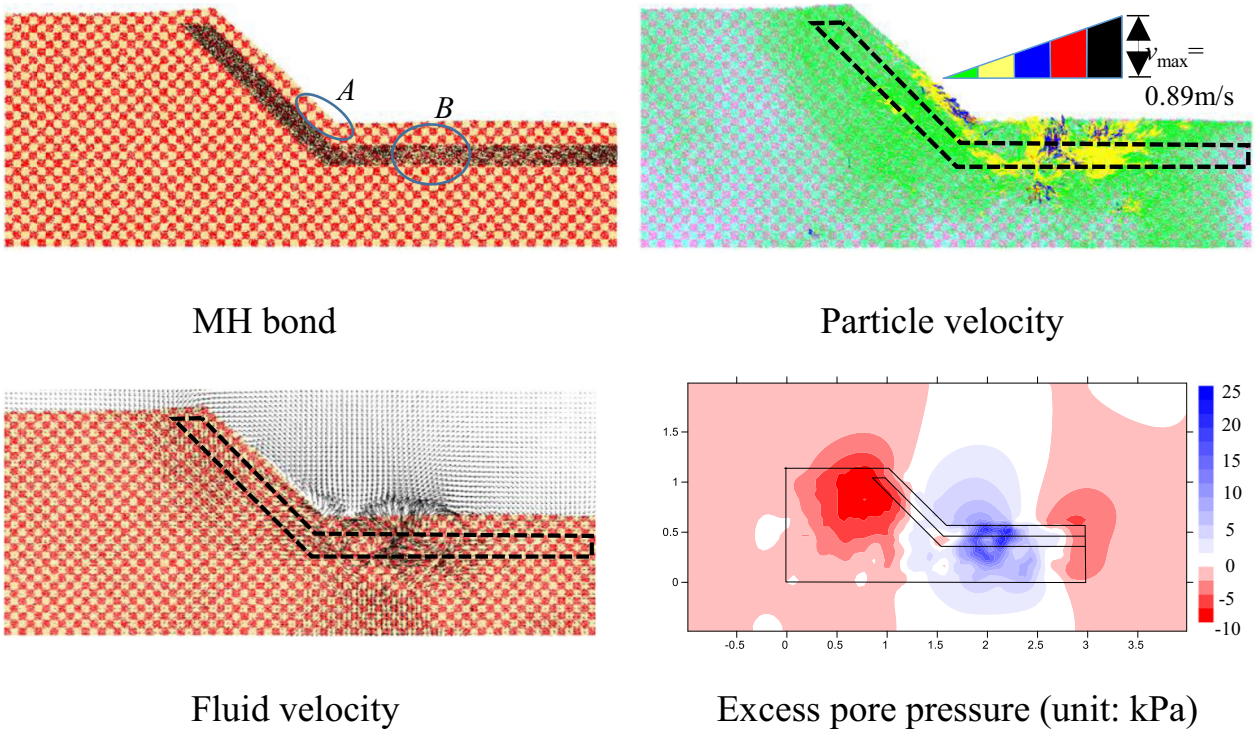

(a) $t = 5$ s

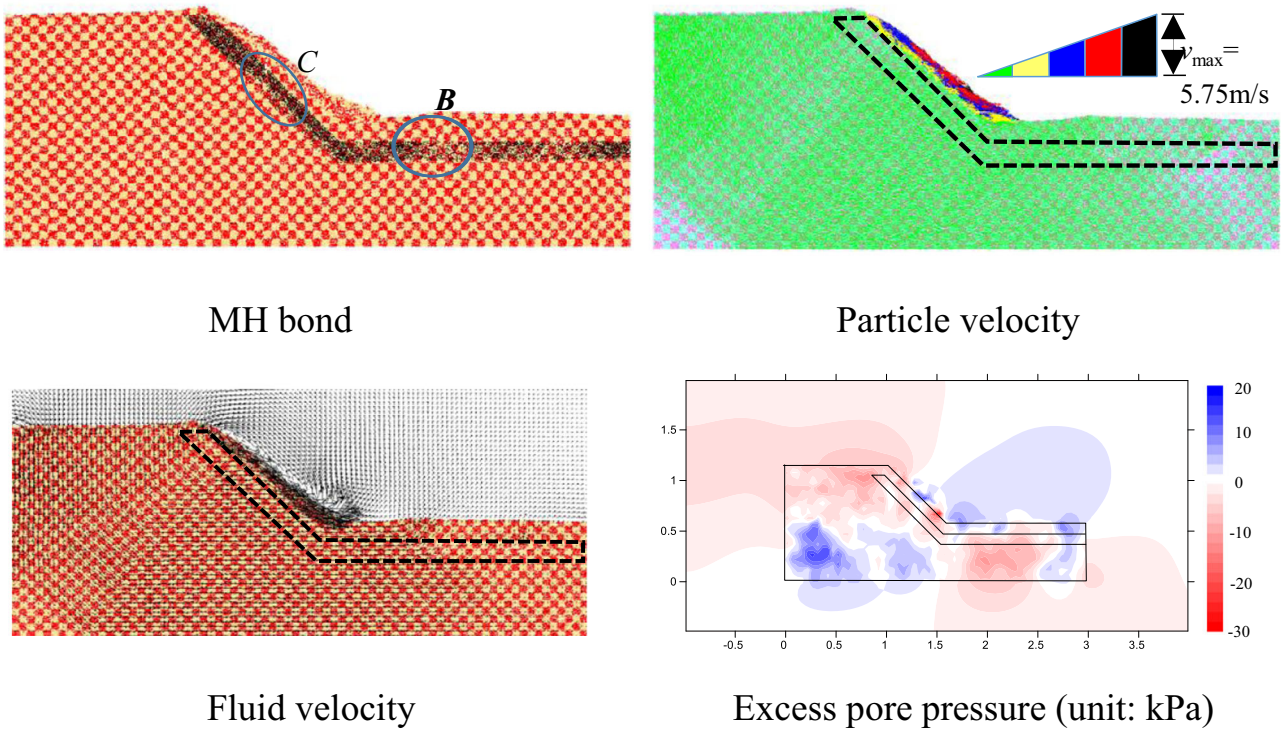

(b) $t = 12$ s

Fig. 9 Spatial distributions of MH bond, particle velocity, fluid velocity, and excess pore water pressure at different elapsed time (MH saturation = 25%)

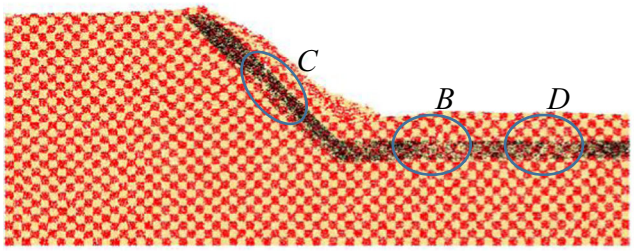

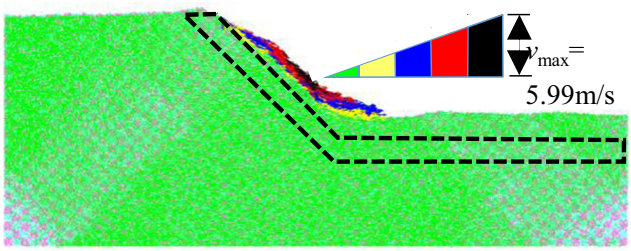

MH bond

Particle velocity

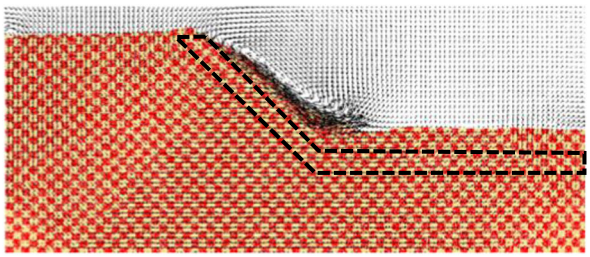

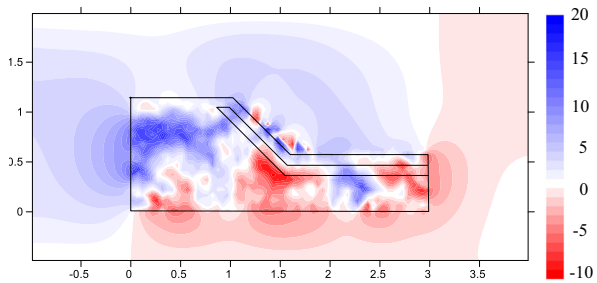

Fluid velocity

Excess pore pressure (unit: kPa)

(c) t = 15 s

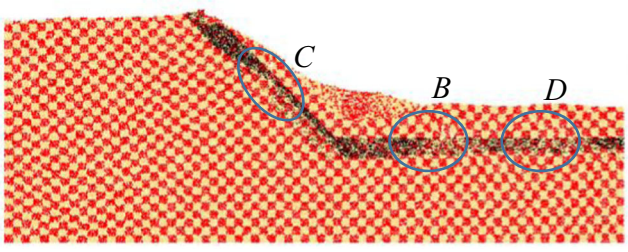

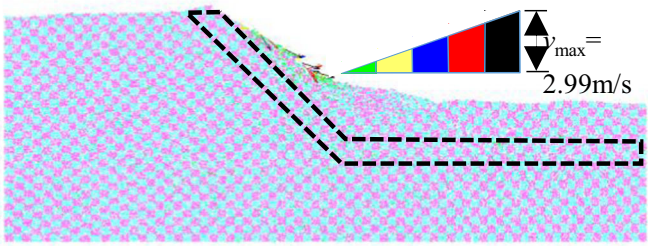

MH bond

Particle velocity

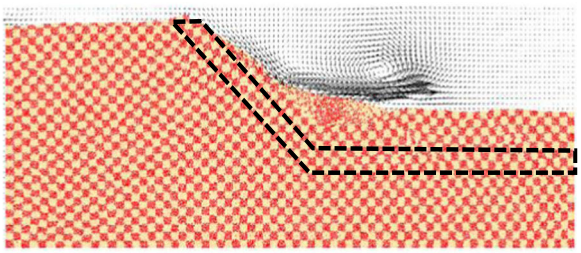

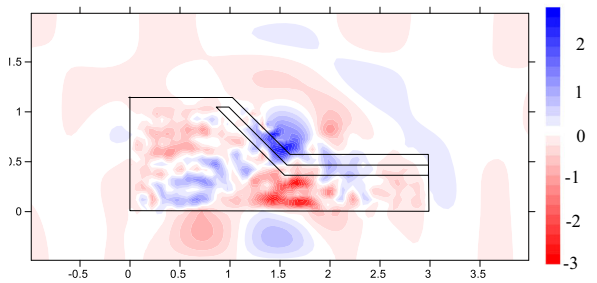

Fluid velocity

Excess pore pressure (unit: kPa)

(d) t = 500 s

Fig. 9 continued.

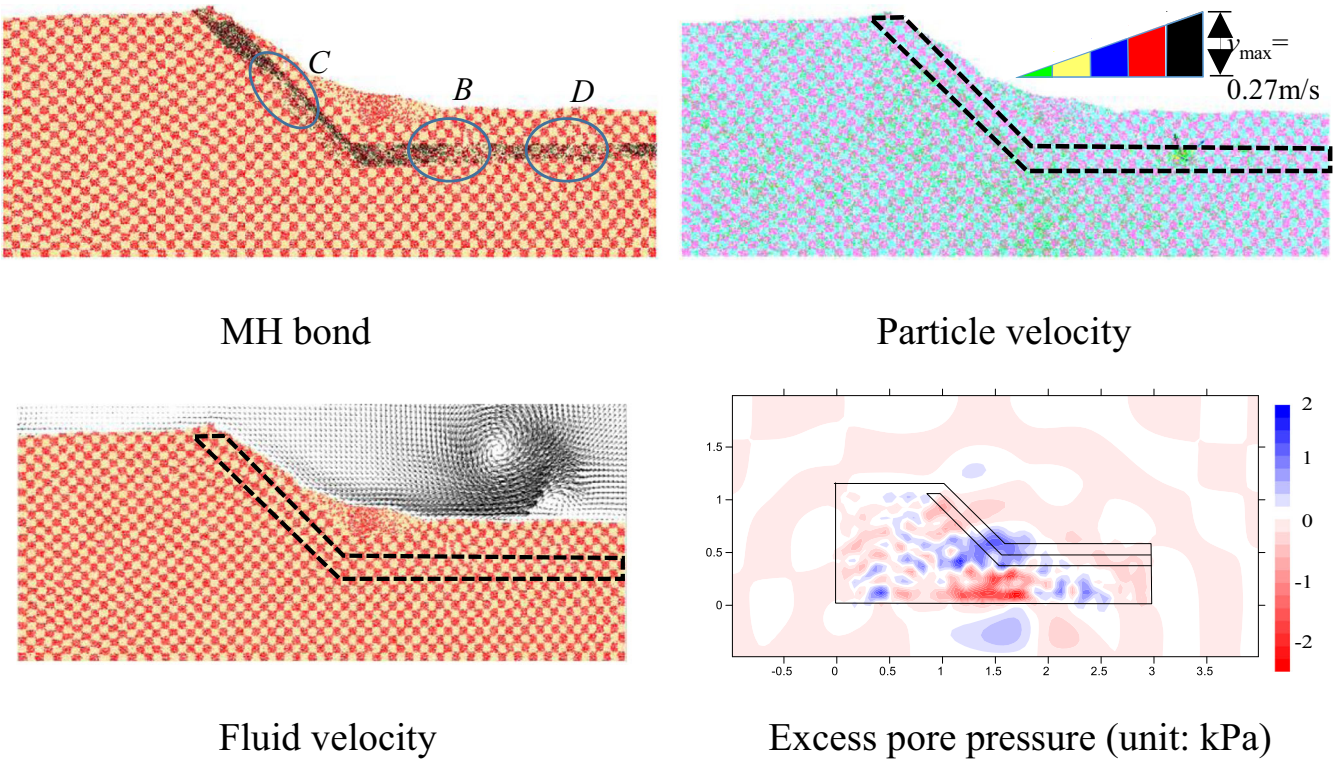

(e) t = 2000 s

Fig. 9 continued.

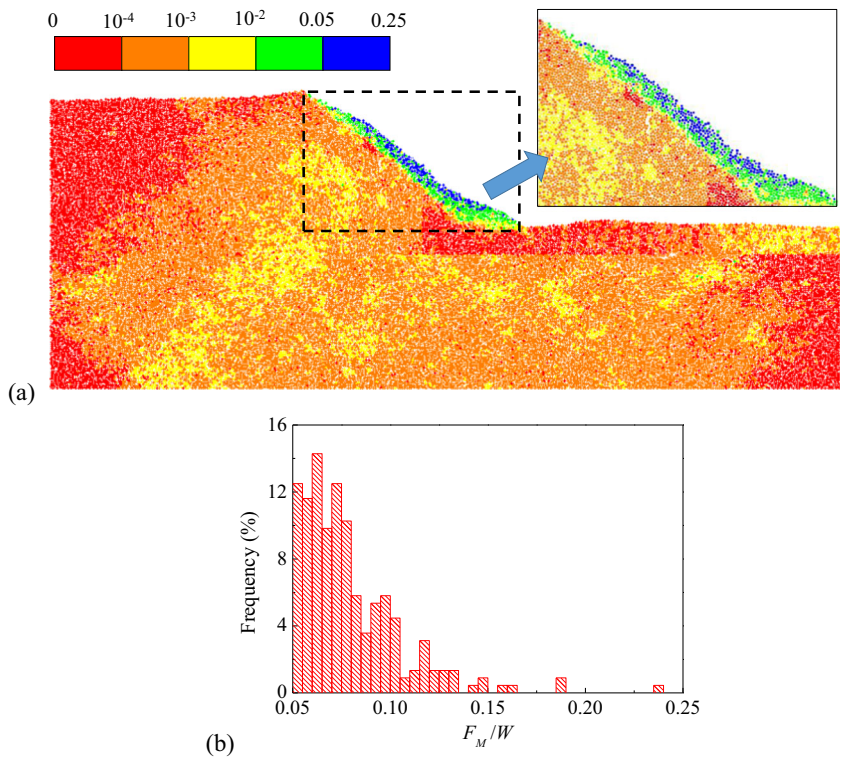

Fig. 10 Distributions of Magnus force. **a** Spatial distribution of normalized Magnus force. **b** Frequency histogram of normalized Magnus force higher than 0.05

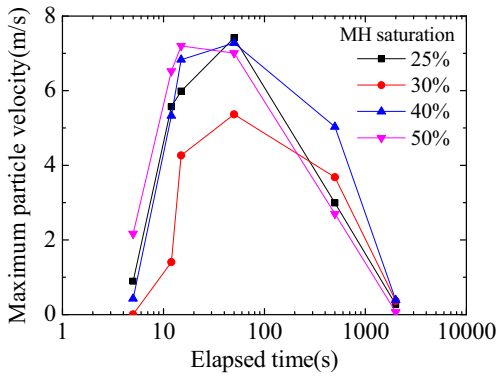

Fig. 11 Maximum particle velocities during landslide for different MH saturations

Deformation and sliding features

Tables 2 and 3 present the seismic loading responses of four slopes with different MH saturations from 30 to 50%, which together with Fig. 9 provide a complete view of the effects of MH saturation from 25 to 50%. Depending on MH saturation, the morphologies of the re-stabilized slopes at $t = 500$ s in Table 2 exhibit different ground deformation and landsliding features in the following three aspects.

(1) Lateral deformation and top surface settlement. The two types of deformation are observed in the two cases with MH saturation of 25 and 30% while no such deformation is present for the other two cases with MH saturation of 40 and 50%. This comparison implies that the top surface settlement results from the lateral deformation of the slope body, instead of resulting from densification of the ground under earthquake loading.

(2) Upheaval. Upheaval in front of the toe is greater in the MH30 case than in the MH25 case, whereas no upheaval is observed for the other two cases.

(3) Re-stabilized slope profile. In the MH25 and MH30 cases, only the top surface layer of particles above the MHBS layer slide downward; in the other two cases with higher MH saturation, particles above the MHBS layer all slide down to the slope toe. The sliding mass volume (area of the smeared part near the original slope toe) generally increases with MH saturation.

Bond breakage

In Table 2, MH bonds are almost intact for MH40 and MH50 cases, whereas significant bond breakage occurs in the other two cases. At $t = 5$ s, bond breakage has already initiated for MH25 case, manifested by the much lower number of bonds in zone B in

Table 2 Evolutions of spatial distribution of MH bond

t	MH saturation=30%	MH saturation=40%	MH saturation=50%
5s			
12s			
15s			
50s			
500s			

Table 3 Evolutions of spatial distribution of particle velocity

t	MH saturation=30%	MH saturation=40%	MH saturation=50%
5s	v_{max}=0.007m/s	v_{max}=0.43m/s	v_{max}=2.17m/s
12s	v_{max}=1.40m/s	v_{max}=5.33m/s	v_{max}=6.52m/s
15s	v_{max}=4.26m/s	v_{max}=6.83m/s	v_{max}=7.20m/s
50s	v_{max}=5.37m/s	v_{max}=7.28m/s	v_{max}=7.01m/s
500s	v_{max}=3.68m/s	v_{max}=5.03m/s	v_{max}=2.70m/s

Fig. 9 than in other areas. At $t = 15$ s, the bond breakage in the inclined MHBS layer becomes significant in zone C for MH25 case. But for the MH30 case, it is until $t = 15$ s that the damaged zone becomes observable in a small zone, and it takes 500 s to develop sufficient bond breakage in the inclined MHBS layer. Although the MH bonding effect is greater in the MH30 case than in the MH25 case, it is not strong enough to resist earthquake and maintain intact as what is observed in the MH40 and MH50 cases. Therefore, the strength of MHBS determined by MH saturation is the key factor to control the bond breakage responses.

Mechanisms behind the seismic loading responses

The above observed MH saturation dependency in slope response is a result of the combined effects of MHBS strength and damping behavior. Experimental results show that MHBS strength and modulus increases with MH saturation but its damping decreases with MH saturation (Kingston et al. 2008; Hyodo et al. 2013). Figure 12 presents the effects of MH saturation on behavior of MHBS simulated in biaxial compression tests with our MH bond contact model. The initial effective confining pressure is 1 MPa, the temperature is 283 K, and the initial pore pressure (back pressure) is 10 MPa. In the drained quasi-static biaxial loading shown in Fig. 12a, the peak and residual strength increases with MH saturation. In the undrained cyclic loading test shown in Fig. 12b–d, a deviator stress of 0.6 MPa was applied with a frequency of 1/36 Hz. The mean slope of the loop E_d (dynamic shear modulus) and the damping ratio λ_d are calculated by

$$E_d = \frac{q_{up} - q_{low}}{\varepsilon_{1,up} - \varepsilon_{1,low}} \tag{11}$$

$$\lambda_d = \frac{A_L}{4\pi A_T} \tag{12}$$

where q_{up} and q_{low} are the upper and lower bounds of the deviator stress, respectively, and $\varepsilon_{1,up}$ and $\varepsilon_{1,low}$ are the corresponding strains. A_L is the area of the hysteretic loop in the q-ε_1 plane and A_T is the area of the triangle ABC in Fig. 12b.

Simulation results in Fig. 12c, d show that the dynamic shear modulus increases with MH saturation while the damping ratio decreases as MH saturation increases. The experimental results can be well predicted qualitatively in our DEM simulations. Due to the two-dimensional nature of the simulation, it is not sought to achieve quantitative consistency between simulation and experiment.

Due the material behavior of MHBS, the effects of MH saturation on submarine landslide induced by seismic loading are twofold:

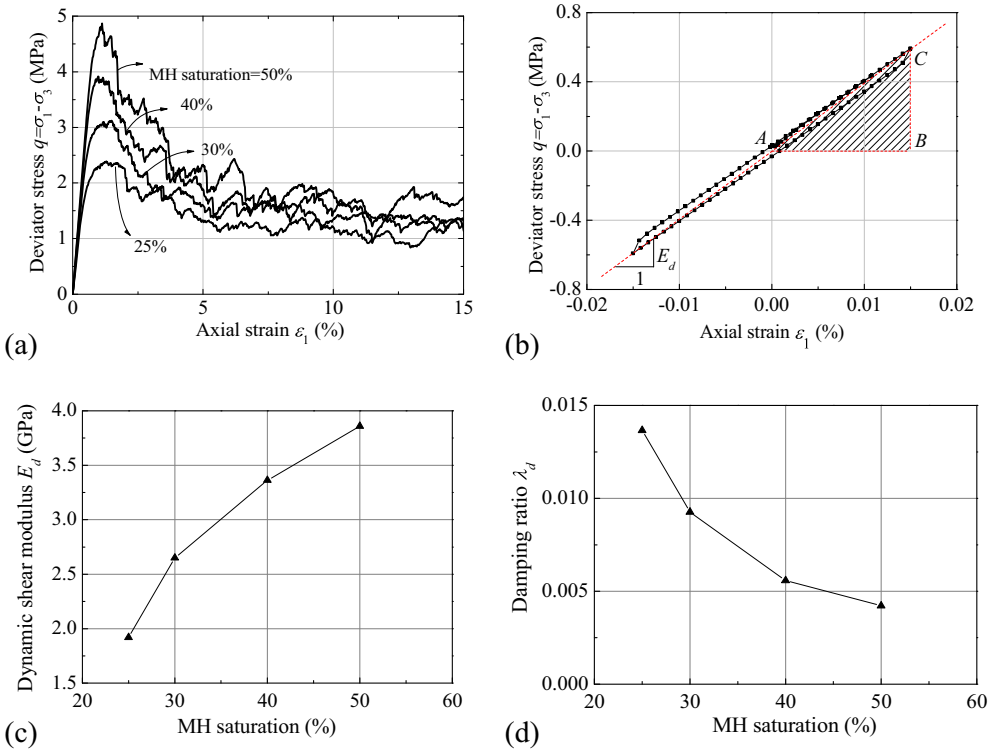

Fig. 12 Effects of MH saturation on behavior of MHBS. **a** Stress-strain curves in drained quasi-static loading. **b** Stress-strain loop in undrained cyclic loading (MH saturation = 25%). **c** Dynamic shear modulus. **d** Damping ratio

(1) Damping effect. With greater MH saturation, the lower damping in MHBS layer allows more energy to be transferred from ground base to potential sliding mass above the MHBS layer along the slope surface. Therefore, the greater disturbance on slope surface due to seismic loading in MH50 case initiates sliding earlier than in the other three cases.

(2) Strength effect. In the MH25 case, the low MHBS strength allows damage onset as early as 5 s after the earthquake starts. The expansion of damaged MHBS zone allows the secondary ground movement patterns including top surface settlement, upheaval, and lateral ground deformation. The slope in MH30 case requires a longer time to accumulate damage in MHBS due to its higher strength than in MH25 case. MHBS in the MH40 and MH50 cases is strong enough to resistance damage due to seismic loading, and therefore, no secondary pattern of deformation is observed in the two cases.>

Discussions and conclusions

The simulated slope is a very simple case compared with the real submarine conditions, and the seismic loading is in a simple sinusoidal pattern with an individual frequency. However, the obtained site responses under seismic loading provide some preliminary insights into submarine landslide hazards. (1) Site conditions. The presence of MH within a specific range of depth beneath the seafloor creates a strong inter-layer. In contrast with the widely studied weak inter-layer site, a strong inter-layer can lead to site responses featured by (a) damage of the strong inter-layer and associated upheaval/settlement deformation (seismic and fluid actions greater than MH bond strength) or (b) strong inter-layer being a rigid bedding layer to amplify the seismic loading, leading to increase in the sliding mass transport (seismic and fluid actions less than MH bond strength). (2) Threat to artificial facilities. Both the primary sliding mass transport and the secondary ground deformation can be hazardous. MH-rich zone may experience a huge movement of sediment along the layer interface between MHBS layer and the overlying sediment. The top surface settlement and upheaval in front of the slope toe suggest a safety distance to be considered to locate oil and gas production platform, pipeline, and cables. Location of artificial facilities needs to consider the hazards of MH melting as well as revealed by Jiang et al. (2015).

In summary, submarine landslide was simulated by coupling the computational fluid dynamics and discrete element method. A dynamic contact model was implemented in the discrete element part to reproduce the dynamic behavior of methane hydrate-bearing sediments. Slight compressibility of fluid was considered in the computational fluid part. Magnus force was incorporated into the fluid-particle interaction, and this force was found to have a significant effect on particle trajectory in the velocity range encountered in submarine landslide.

A sinusoidal type seismic loading was applied to bring the simulated submarine slope to failure under different MH saturations. A flow-type sliding is observed and the sliding ends with a gentle slope of accumulated debris material. The fluid flows in an eddy pattern near the sliding mass: water flows upward from slope toe to crest above the slope surface and in the opposite direction below the slope surface. The regain of slope stability is

accompanied by a slope-height sized round fluid eddy traveling away from the slope.

MH saturation influences the initiation of landslide, sliding process, and final deposition. In the two cases with MH saturation = 25 and 30%, under the combined seismic loading and particle-fluid interaction, MHBS layer damage initiates in front of the slope toe and then occurs at the mid-slope in succession. The development of MHBS damage allows seismic and fluid loads to cause secondary ground movements: top ground surface settlement behind the slope crest and ground upheaval in front of the slope toe. In the two cases with greater MH saturation (40 and 50%), no such secondary ground movement is observed because the seismic and fluid loads are not strong enough to damage the MHBS layer. With greater MH saturation, the lower damping in MHBS layer allows more energy to be transferred from ground base to potential sliding mass. Consequently, the MH saturation case sliding initiates earlier in the 50% MH saturation case than in the other three cases. The observed effects of MH saturation originate from the increase of strength and decrease of damping of MHBS as MH saturation increases.

Seismic site response depends on site geometry, sediment property, and the input seismic loading (vibration intensity and frequency component). Refined simulation need to be run in future work to consider in situ slope morphology, realistic permeability, strength and damping of sediment, and seismic input from history record.

Acknowledgements

The authors would like to thank Mr. Chao Sun, the first author's former MSc student, for his contribution in numerical simulation. FundingThe research is funded by Key Program of National Natural Science Foundation of China with Grant No. 51639008 and Foundation for Research Initiation at Nanjing Tech University with Grant No. 3827401759, which are sincerely appreciated.

References

Bains S, Corfield RM, Norris RD (1999) Mechanisms of climate warming at the end of the Paleocene. Science 285(5428):724–727

Barkla H, Auchterlonie L (1971) The Magnus or robins effect on rotating spheres. J Fluid Mech 47(3):437–447

Bea RG (1971) How sea floor slides affect offshore structures. Oil Gas J 69(48):88–92

Bice KL, Marotzke J (2002) Could changing ocean circulation have destabilized methane hydrate at the Paleocene/Eocene boundary? Paleoceanography 17(2):8.1–8.12

Biscontin G, Pestana JM, Nadim F (2004) Seismic triggering of submarine slides in soft cohesive soil deposits. Mar Geol 203(3):341–354

Boswell R, Collett TS (2011) Current perspectives on gas hydrate resources. Energy Environ Sci 4(4):1206–1215

Dvorkin J, Prasad M, Sakai A, Lavoie D (1999) Elasticity of marine sediments: rock physics modeling. Geophys Res Lett 26(12):1781–1784

Ebinuma T, Kamata Y, Minagawa H, Ohmura R, Nagao J, Narita H (2005) Mechanical properties of sandy sediment containing methane hydrate. Proceeding of 5th International Conference on Gas Hydrates, pp 958–961

El-Robrini M, Gennesseaux M, Mauffret A (1985) Consequences of the El-Asnam earthquakes: turbidity cur-rents and slumps on the Algerian margin (western Mediter-ranean). Geo-Mar Lett 5(3):171–176

Fine IV, Rabinovich AB, Bornhold BD, Thomson RE, Kulikov EA (2005) The grand banks landslide-generated tsunami of November 18, 1929: preliminary analysis and numerical modeling. Mar Geol 215(1–2):45–57

Goff J, Terry JP (2016) Tsunamigenic slope failures: the Pacific Islands 'blind spot'? Landslides 13(6):1535–1543

Harbitz C (1992) Model simulations of tsunamis generated by the Storegga slides. Mar Geol 105(1–4):1–21

Hasegawa HS, Kanamori H (1987) Source mechanism of the magnitude 7.2 Grand Banks earthquake of November 1929: Double couple or submarine landslide? Bull Seismol Soc Am 77(6):1984–2004

Heezen BC, Drake CL (1964) Grand banks slump. AAPG Bull 48(2):221–225

Heezen BC, Ewing M (1955) Orléansville earthquake and turbidity currents. AAPG Bull 39(12):2505–2514

Hsu SK, Kuo J, Lo CL, Tsai CH, Doo WB, Ku CY, Sibuet JC (2008) Turbidity currents, submarine landslides and the 2006 Pingtung earthquake off SW Taiwan. Terr Atmos Ocean Sci 19(6):767–772

Hyodo M, Nakata Y, Yoshimoto N, Fukunaga M, Kubo K, Nanjo Y, Matsuo T, Nakamura K (2002) Triaxial compressive strength of methane hydrate. Proceedings of the 12th international offshore and polar engineering conference, Japan, pp 26–31

Hyodo M, Nakata Y, Yoshimoto N, Ebinuma T (2005) Basic research on the mechanical behavior of methane hydrate-sediments mixture. Soils Found 45(1):75–85

Hyodo M, Yoneda J, Yoshimoto N, Nakata Y (2013) Mechanical and dissociation properties of methane hydrate-bearing sand in deep seabed. Soils Found 53(2):299–314

Imre B, Räbsamen S, Springman S (2008) A coefficient of restitution of rock materials. Comput Geosci 34(4):339–350

Jiang M, Liu J, Kwok CY, Shen Z (2018a) Exploring the undrained cyclic behavior of methane-hydrate-bearing sediments using CFD–DEM. Comptes Rendus Mécanique. https://doi.org/10.1016/j.crme.2018.05.007

Jiang MJ, Yu HS, Harris D (2005) A novel discrete model for granular material incorporating rolling resistance. Comput Geotech 32(5):340–357

Jiang MJ, Zhu FY, Liu F, Utili S (2014) A bond contact model for methane hydrate bearing sediments with interparticle cementation. Int J Numer Meth Eng 38(17):1823–1854

Jiang MJ, Sun C, Crosta GB, Zhang WC (2015) A study of submarine steep slope failures triggered by thermal dissociation of methane hydrates using a coupled CFD-DEM approach. Eng Geol 190(3):1–16

Jiang MJ, He J, Wang JF, Chareyre B, Zhu FY (2016) DEM analysis of geomechanical properties of cemented methane hydrate bearing soils at different temperatures and pore pressures. Int J Geomech 16(3):04015087

Jiang MJ, Liu J, Shen ZF, Xi BL (2018b) Exploring the critical state properties and major principal stress rotation of sand in direct shear test using the distinct element method. Granul Matter 20(2):25. https://doi.org/10.1007/s10035-018-0796-z

Kingston E, Priest J, Clayton CRI, Best A (2006) Gas hydrate growth morphologies and their influence on the geophysical properties of a hydrate bearing sand. Presentation in Sediment Hosted Gas Hydrate Conference, London

Kingston E, Clayton C, Priest J (2008) Gas hydrate growth morphologies and their effect on the stiffness and damping of a hydrate bearing sand. Proceedings of the 6th International Conference on Gas Hydrates, pp 2008

Kvenvolden KA, Lorenson TD (2001) The global occurrence of natural gas hydrate. In: Paull CK, Dillon WP (Eds.) Natural gas hydrates: occurrence, distribution, and detection. American Geophysical Union, pp 3–18

Locat J, Lee HJ (2002) Submarine landslides: advances and challenges. Can Geotech J 39(39):193–212

Locat J, Lee HJ, Locat P, Imran J (2004) Numerical analysis of the mobility of the Palos Verdes debris avalanche, California, and its implication for the generation of tsunamis. Mar Geol 203(3):269–280

Lopez-Venegas AM, Brink US, Geist EL (2008) Submarine landslide as the source for the October 11, 1918 Mona passage tsunami: observations and modeling. Mar Geol 254(1):35–46

Luo M, Wang H, Yang S, Chen D (2013) Research advancement of natural gas hydrate in South China Sea. Bull Mineral Petrol Geochem 32(1):56–69

Masson DG, Huggett QJ, Brunsden D (1993) The surface texture of the Saharan debris flow deposit and some speculations on submarine debris flow processes. Sedimentology 40(3):583–598

Masson DG, Harbitz CB, Wynn RB, Pedersen G, Løvholt F (2006) Submarine landslides: processes, triggers and hazard prediction. Philos Trans A Math Phys Eng Sci 364(1845):2009–2039

Masui A, Haneda H, Ogata Y, Aoki K (2005) Effects of methane hydrate formation on shear strength of synthetic methane hydrate sediments. Proceedings of the 5th international offshore and polar. Eng Conf:364–369

McAdoo BG, Pratson LF, Orange DL (2000) Submarine landslide geomorphology, US continental slope. Mar Geol 169(1–2):103–136

Mienert J, Vanneste M, Bünz S, Andreassen K, Haflidason H, Sejrup HP (2005) Ocean warming and gas hydrate stability on the mid-Norwegian margin at the Storegga slide. Mar Pet Geol 22(1):233–244

Miyazaki K, Masui A, Sakamoto Y, Aoki K, Tenma N, Yamaguchi T (2011) Triaxial compressive properties of artificial methane-hydrate-bearing sediment. J Geophys Res 116(B6):309–311

Nabeshima Y, Takai Y, Komai T (2005) Compressive strength and density of methane hydrate. Proceedings of the 6th ISOPE Ocean Mining Symposium, pp. 199–202
Rubinow S, Keller JB (1961) The transverse force on a spinning sphere moving in a viscous fluid. J Fluid Mech 11(3):447–459
Shamy UE, Denissen C (2010) Microscale characterization of energy dissipation mechanisms in liquefiable granular soils. Comput Geotech 37(7–8):846–857
Shamy UE, Zeghal M (2007) A micro-mechanical investigation of the dynamic response and liquefaction of saturated granular soils. Soil Dyn Earthq Eng 27(8):712–729
Shen ZF, Jiang MJ (2016) DEM simulation of bonded granular material. Part II: extension to grain-coating type methane hydrate bearing sand. Comput Geotech 75:225–243
Solheim A, Berg K, Forsberg C, Bryn P (2005) The Storegga slide complex: repetitive large scale sliding with similar cause and development. Mar Pet Geol 22(1):97–107
Song YC, Yu FL, Y H, Liu WG, Zhao JF (2010) Mechanical property of artificial methane hydrate under triaxial compression. J Nat Gas Chem 19(3):246–250
Svensen H, Planke S, Malthe-Sørenssen A, Jamtveit B, Myklebust R, Eidem TR, Rey SS (2004) Release of methane from a volcanic basin as a mechanism for initial Eocene global warming. Nature 429(6991):542–545
Tappin DR, Watts P, McMurtry GM, Lafoy Y, Matsumoto T (2001) The Sissano, Papua New Guinea tsunami of July 1998—offshore evidence on the source mechanism. Mar Geol 175(1–4):1–23
Thornton C, Cummins SJ, Cleary PW (2013) An investigation of the comparative behaviour of alternative contact force models during inelastic collisions. Powder Technol 233(3):30–46
Tréhu AM, Bohrmann G, Rack FR et al (2003) Proceedings of the Ocean Drilling Program, Initial Reports, Vol 204
Tsuji Y, Morikawa Y, Mizuno O (1985) Experimental measurement of the Magnus force on a rotating sphere at low Reynolds numbers. J Fluid Eng 107(4):484–488
Uri S, Lee HJ, Geist EL, Twichell D (2009) Assessment of tsunami hazard to the US East Coast using relationships between submarine landslides and earthquakes. Mar Geol 264(1):65–73
Valdes JR, Santamarina JC (2007) Particle transport in a nonuniform flow field: retardation and clogging. Appl Phys Lett 90(24):244101
Winters WJ, Waite WF, Mason D, Gilbert L, Pecher I (2007) Methane gas hydrate effect on sediment acoustic and strength properties. J Pet Sci Eng 56(1–3):127–135
Wright SG, Rathje EM (2003) Triggering mechanisms of slope instability and their relationship to earthquakes and tsunamis. Pure Appl Geophys 160(10–11):1865–1877
Yavari-Ramshe S, Ataie-Ashtiani B (2017) A rigorous finite volume model to simulate subaerial and submarine landslide-generated waves. Landslides 14(1):203–221
Yu F, Song YC, Liu WG, Li YH, Zhao JF (2010) Study on shear strength of artificial methane hydrate. Proceedings of the ASME 29th international conference on ocean, Offshore and Arctic Engineering, Shanghai, pp 705–710
Zhang L, Luan XW (2013) Stability of submarine slopes in the northern South China Sea: a numerical approach. Chin J Oceanol Limnol 31(1):146–158
Zhou Q, Fan LS (2015) Direct numerical simulation of moderate-Reynolds-number flow past arrays of rotating spheres. Phys Fluids 27(7):073306
Zhou J, Wang Z, Chen X, Zhang J (2014) Uplift mechanism for a shallow-buried structure in liquefiable sand subjected to seismic load: centrifuge model test and DEM modeling. Earthq Eng Eng Vib 13(2):203–214

M. Jiang
School of Civil Engineering,
Tianjin University,
Tianjin, 300072, China

M. Jiang
State Key Laboratory for Disaster Reduction in Civil Engineering,
Tongji University,
Shanghai, 200092, China

M. Jiang
Key Laboratory of Geotechnical and Underground Engineering of Ministry of Education,
Tongji University,
Shanghai, 200092, China

M. Jiang · D. Wu
Department of Geotechnical Engineering, College of Civil Engineering,
Tongji University,
Shanghai, 200092, China

Z. Shen (✉)
Institute of Geotechnical Engineering,
Nanjing Tech University,
Nanjing, 210009, China
Email: zhifu.shen@njtech.edu.cn